

## Insight into Kondo screening in the intermediate-valence compound $\text{SmOs}_4\text{Sb}_{12}$ uncovered by soft x-ray magnetic circular dichroism

Y. Saitoh,<sup>1,\*</sup> H. Fujiwara,<sup>2</sup> A. Yasui,<sup>3</sup> T. Kadono,<sup>4</sup> H. Sugawara,<sup>5</sup> D. Kikuchi,<sup>6</sup> H. Sato,<sup>6</sup> S. Suga,<sup>7</sup> A. Yamasaki,<sup>8</sup> A. Sekiyama,<sup>2</sup> and S. Imada<sup>4</sup>

<sup>1</sup>Materials Sciences Research Center, Japan Atomic Energy Agency (JAEA), Sayo, Hyogo 679-5148, Japan

<sup>2</sup>Graduate School of Engineering Science, Osaka University, Toyonaka, Osaka 560-8531, Japan

<sup>3</sup>Japan Synchrotron Radiation Research Institute (JASRI), Sayo, Hyogo 679-5198, Japan


<sup>4</sup>Department of Physical Sciences, Ritsumeikan University, Kusatsu, Shiga 525-8577, Japan

<sup>5</sup>Graduate School of Science, Kobe University, Kobe, Hyogo 657-8501, Japan

<sup>6</sup>Graduate School of Science, Tokyo Metropolitan University, Hachioji, Tokyo 192-0397, Japan

<sup>7</sup>Institute of Scientific and Industrial Research, Osaka University, 8-1 Mihogaoka, Ibaraki 567-0047, Japan

<sup>8</sup>Faculty of Science and Engineering, Konan University, Kobe 658-8501, Japan

 (Received 29 January 2020; revised 12 October 2020; accepted 13 October 2020; published 29 October 2020)

Through a high-precision soft x-ray magnetic circular dichroism (XMCD) study of the intermediate-valence compound  $\text{SmOs}_4\text{Sb}_{12}$ , we show our successful approach of revealing unprecedented details of Kondo screening below a characteristic temperature of  $T_0 \sim 20$  K in the paramagnetic phase. The multiplet XMCD structure at the Sm  $M_5$  edge sensitive to the  $4f$  configuration enabled us to observe a clear difference between the temperature evolution above and below  $T_0$  with one- and two-component behavior, respectively. Our findings are in strong contrast to the conventional Kondo crossover that coincides with the valence transition, but are qualitatively accounted for by theoretical XMCD predictions combined with the two-fluid phenomenology recently proposed. This work contributes to the large context of Kondo physics that is closely related to quantum criticality in heavy fermion systems.

DOI: [10.1103/PhysRevB.102.165152](https://doi.org/10.1103/PhysRevB.102.165152)

### I. INTRODUCTION

Materials containing partially filled  $f$  orbitals, frequently called Kondo lattices (KLs), have been studied extensively for several decades. At low temperatures, KLs display a large variety of physical phenomena, including magnetic order, intermediate valence (IV), heavy fermion (HF), non-Fermi-liquid behavior, and unconventional superconductivity [1], which are associated with quantum criticality [2]. A comprehensive understanding of quantum phase transitions has been a central topic in strongly correlated electron systems [3]. The ground states of KLs are usually governed by a delicate balance between the intersite Ruderman-Kittel-Kasuya-Yosida (RKKY) and on-site Kondo interactions as conceptually described by the well-known Doniach diagram [1,2,4]. The RKKY interaction tends to dictate the long-range antiferromagnetism. The Kondo interaction favors a nonmagnetic singlet ground state involving the local moment and conduction electrons to form itinerant states with enhanced effective mass and susceptibility [1,2].

One of the key features of KLs is the temperature evolution of the  $f$  states from local-moment paramagnetic behavior at high temperatures to various types of ground states, in which the local moment and itinerant degrees of freedom are entangled [5–10]. Since a complete theoretical

description of KLs remains elusive, the Anderson impurity model (AIM) has been most widely applied to describe the thermodynamic and spectroscopic properties of KLs [11–13]. Recent studies, by contrast, have shown that a large number of experimental quantities are well captured by a phenomenological two-fluid description [14,15]. This model offers a constructive way of understanding complicated states of KLs in place of the mean-field Doniach model. However, microscopic experimental evidence is highly required to understand the underlying physics of the two-fluid phenomenology [16].

$\text{SmOs}_4\text{Sb}_{12}$  in the filled skutterudite family exhibits a heavy Fermi liquid state, with a Sommerfeld coefficient of  $\gamma \approx 0.82$  J/(mol K<sup>2</sup>), along with ferromagnetic order below the Curie temperature of  $T_C \approx 2.6$  K with a small ordered moment of only  $\approx 0.02 \mu_B/\text{Sm}$  under ambient pressure [17–19]. This HF state is unusually robust against applied magnetic fields up to 14 T [17,20], as in some Sm-based caged compounds [21]. In addition, this material, with all the Sm sites being crystallographically equivalent, is characterized by strong IV between  $\text{Sm}^{2+}$  ( $4f^6$ ) and  $\text{Sm}^{3+}$  ( $4f^5$ ) even at room temperature [20–23]. The Sm valence gradually shifts toward  $\text{Sm}^{2+}$  down to a characteristic temperature of  $T_0 = 20\text{--}25$  K, while a nuclear quadrupole resonance (NQR) study suggests the distinct onset of Kondo screening below  $T_0$  [24,25]. Such behavior contrasts with the conventional picture of the Kondo effect [1,2,26]. In addition, this picture has recently been questioned in the temperature scale of the valence in Yb KLs [27,28]. The microscopic details of the physical properties

\*ysaitoh@spring8.or.jp

of  $\text{SmOs}_4\text{Sb}_{12}$  have been an important subject of continued studies [21,29].

X-ray magnetic circular dichroism (XMCD) in x-ray absorption spectroscopy (XAS) at the rare earth  $M_{4,5}$  edges (excitation of  $3d$  core levels) reflects the dipole allowed transitions from the  $3d^{10}4f^n$  initial state to the  $3d^94f^{n+1}$  final states. Such final states show pronounced multiplet effects determined by  $n$ , thereby offering an excellent element-specific tool for the characterization of the rare earth  $4f$  states [30–32]. Recent advances have allowed the application of XMCD spectroscopy to study the Kondo effect in dilute Fe impurities in Cu films [33] and  $\text{CePt}_5/\text{Pt}(111)$  [34]. The Kondo effect is found to be reflected in the XMCD shape in Ref. [33], but not in Ref. [34]. Recently Nanba *et al.* [35] have theoretically predicted a clear difference in the Sm  $M_5$  XMCD line shape between a magnetic and nonmagnetic IV ground states of  $\text{SmOs}_4\text{Sb}_{12}$ . We have perceived these ground states as a kind of the dichotomic two fluids, which provides a guide to the present study.

We report here the results of a high-precision XMCD study at the Sm  $M_5$  edge of  $\text{SmOs}_4\text{Sb}_{12}$ . We show that the XMCD is extremely sensitive to the temperature evolution of the Sm  $4f$  magnetic state across  $T_0$ , which exceeds what has been expected for soft x-ray core-level spectroscopies with the natural linewidth on the order of several hundred meV. We discuss these results in reference to the spectral predictions and the two-fluid model. We have observed additional XMCD features that develop below  $T_0$ , which have its origin in the Kondo singlet. Our results constitute a detailed investigation of the temperature-dependent Kondo entanglement in  $\text{SmOs}_4\text{Sb}_{12}$ , and provide microscopic information at the heart of the two-fluid model.

## II. EXPERIMENT

The XAS and XMCD measurements were performed on BL23SU at the SPring-8 synchrotron radiation (SR) facility using a superconducting magnet in combination with the 1 Hz photon helicity switching mode [36]. Here the XMCD is defined as the difference between the XAS spectra for parallel ( $\mu_+$ ) and antiparallel ( $\mu_-$ ) alignment of the photon helicity and the magnetic field ( $H$ ), as in the case of our previous study on  $\text{CeFe}_2$  [37]. All the XMCD spectra were obtained in total electron yield mode with a beam spot diameter of  $\sim 0.2$  mm under  $H = \pm 7$  T along the incident beam direction, which is parallel to the cubic [001] direction of a high-quality single crystal [17]. A single crystal of paramagnetic SmS (001) was also measured at 10 K as a standard sample with a  $\text{Sm}^{2+}$  valence state [38,39]. The XMCD spectra were measured immediately after cleaving the samples in ultrahigh vacuum. The energy resolution was set to better than 0.15 eV. In order to minimize experimental artifacts arising from system errors, each XMCD spectrum was measured for opposite orientations of the applied magnetic field and the resulting two spectra were averaged.

## III. RESULTS AND DISCUSSION

### A. Experimental observations

Figures 1(a) and 1(b) present the polarization averaged XAS [ $(\mu_- + \mu_+)/2$ ], and XMCD ( $\mu_- - \mu_+$ ) spectra,

respectively, obtained at the Sm  $M_5$  absorption edge of  $\text{SmOs}_4\text{Sb}_{12}$  at  $T = 5.5 (\pm 0.5)$  and  $50 (\pm 0.2)$  K across  $T_0$  in the paramagnetic phase. The XAS spectra of  $\text{SmOs}_4\text{Sb}_{12}$  are quite similar to that at 20 K in Ref. [22]. For comparison, the XAS and XMCD spectra of SmS, together with those of  $\text{Sm}_{0.982}\text{Gd}_{0.018}\text{Al}_2$ , labeled as (Sm,Gd) $\text{Al}_2$ , at 45 K [40] are shown in Figs. 1(d) and 1(e) as a  $\text{Sm}^{2+}$  and  $\text{Sm}^{3+}$  reference spectra, respectively. The small XAS shoulder labeled as A, and the small peak at 1072.6 eV in Fig. 1(a) are ascribed to  $\text{Sm}^{2+}$  components.

A closer examination of Fig. 1(a) shows a small difference in the intensity ratio of peak B to A ( $I_B/I_A$ ), indicating that the Sm valence in  $\text{SmOs}_4\text{Sb}_{12}$  slightly shifts toward  $\text{Sm}^{2+}$  with decreasing temperature. Since the considerable overlap between the  $\text{Sm}^{2+}$  and  $\text{Sm}^{3+}$  features complicates the quantitative determination of the Sm valence, we plot  $I_B/I_A$  as a function of temperature (left axis) in Fig. 1(f), and compare it with previous experimental results of the Sm valence (right axis) determined by bulk sensitive SR-based techniques of XAS at the Sm  $L_2$  edge [20] and Sm  $3d$  hard x-ray photoemission spectroscopy (HAXPES) [22]. Our XAS results are basically consistent with those bulk behavior.

More importantly, the XMCD shape in Fig. 1(b) exhibits distinct changes, which are most pronounced at negative peak E, and also at positive peaks C and F. Note that the spectra are scaled for ease of a visual comparison. Figure 1(c) incorporates the XMCD spectra at intermediate temperatures of 10 and 25 K. As can be typically seen from the peak E intensity, the XMCD shape shows little change between 50 and 25 K above  $T_0$ , followed by an unusual significant progressive development below  $T_0$  without any appreciable change in the Sm valence [Fig. 1(f)].

A fundamental understanding of the complicated XMCD signals is offered by the reference XMCD spectra as indicated in Fig. 1(e). Note here that  $\text{Sm}^{2+}$  and  $\text{Sm}^{3+}$  free ions have nonmagnetic and magnetic Hund's rules ground states with total angular momenta of  $J = 0$  (singlet) and  $5/2$ , respectively.

The temperature-independent XMCD shape observed above  $T_0$  is typical of materials consisting of local magnetic moments, and is largely dominated by  $\text{Sm}^{3+}$  in character. This XMCD shape remains below  $T_0$  with constant relative intensities for the multiplet D, G, and H features. The additionally enhanced XMCD intensities for three peaks C, E, and F below  $T_0$  are commonly ascribed to the contribution from  $\text{Sm}^{2+}$ , although the  $\text{Sm}^{2+}$  component of G' is missing. In other words, some of the  $\text{Sm}^{2+}$  XMCD components are selectively enhanced below  $T_0$  in  $\text{SmOs}_4\text{Sb}_{12}$ . It also turns out that a weighted sum of the reference  $\text{Sm}^{2+}$  and  $\text{Sm}^{3+}$  XMCD spectra cannot accommodate the experimental G/H intensity ratio of larger than 1 that is independent of temperature. A similar finding holds for the XMCD at the Sm  $M_4$  edge as shown in Fig. 2, where the Sm  $M_{4,5}$  XAS and XMCD spectra of  $\text{SmOs}_4\text{Sb}_{12}$  at 5.5 K are displayed, and the XMCD spectrum is compared with the XMCD spectra of the  $\text{Sm}^{2+}$  and  $\text{Sm}^{3+}$  reference samples.

Figure 1(g) compares the temperature dependence of the bulk susceptibility  $\chi$  (right axis, solid and dashed red curves) [18] with the XMCD intensity of peaks E and G each scaled to  $\chi$  at 50 K. Bulk magnetization isotherms in  $\text{SmOs}_4\text{Sb}_{12}$  are linear in the external field up to 7 T above  $\approx 5$  K [18,41].

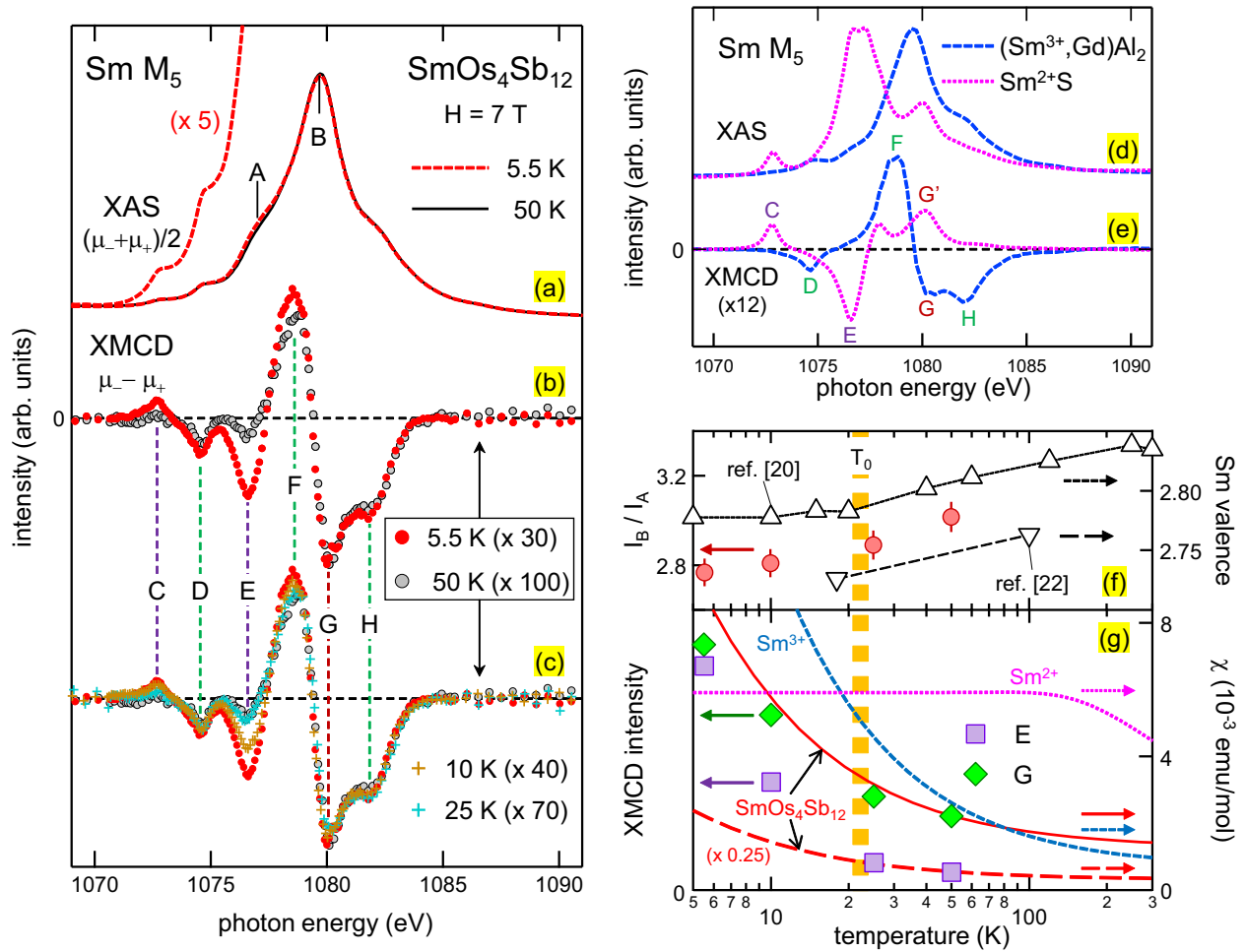


FIG. 1. Sm  $M_5$  (a) XAS and (b) XMCD spectra at temperatures of 5.5 and 50 K, and (c) XMCD spectra in the temperature range of 5.5–50 K of  $\text{SmOs}_4\text{Sb}_{12}$  under a magnetic field of 7 T. Sm  $M_5$  (d) XAS and (e) XMCD spectra for a  $\text{Sm}^{2+}$  and  $\text{Sm}^{3+}$  reference compounds of  $\text{SmS}$  and  $(\text{Sm},\text{Gd})\text{Al}_2$  [40], respectively. (f) Temperature dependence of the XAS intensity ratio of peaks B to A in (a) (full circles, left axis) compared with the Sm valence (right axis) previously determined in Refs. [20,22]. (g) Temperature dependence of the XMCD amplitude of features E and G in (c) (full markers, left axis) compared with the magnetic susceptibility  $\chi$  of  $\text{SmOs}_4\text{Sb}_{12}$  [18] (right axis). Also shown are free ion  $\chi$  curves for  $\text{Sm}^{2+}$  and  $\text{Sm}^{3+}$  [42] by dotted curves.

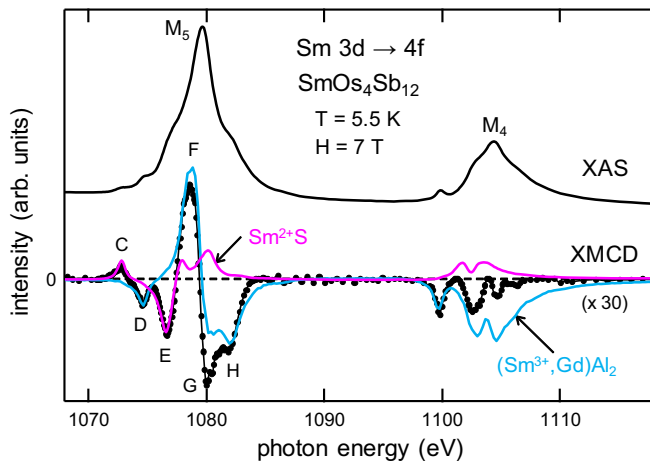


FIG. 2. Sm  $M_{4,5}$  XAS and XMCD spectra of  $\text{SmOs}_4\text{Sb}_{12}$  measured at 5.5 K under 7 T. Also shown are  $\text{Sm}^{2+}$  and  $\text{Sm}^{3+}$  [40] XMCD reference spectra for comparison.

It is clear that the two features show a different dependence on temperature: the peak E intensity fails to track  $\chi$  with a positive deviation below  $T_0$ , while the peak G intensity roughly proportional to  $\chi$  shows a clear negative deviation at the lowest temperature measured. In Fig. 1(g), free ion  $\chi$  curves calculated for  $\text{Sm}^{2+}$  and  $\text{Sm}^{3+}$  [42] are included for comparison. Although peak E originates from  $\text{Sm}^{2+}$ , its magnetic behavior is different than that of  $\text{Sm}^{2+}$  characterized by a temperature-independent Van Vleck paramagnetism at low temperatures [38]. These results again illustrate that the unusual temperature evolution across  $T_0$  cannot be described by a simple picture of the incoherent or temporal fluctuation between  $\text{Sm}^{2+}$  and  $\text{Sm}^{3+}$ . This equally indicates that our findings are irrelevant to impurity and surface effects generally dominated by  $\text{Sm}^{3+}$  contributions [22,43]. Such a simple fluctuation picture has frequently been invoked for IV compounds [21,44], although it cannot describe heavy fermions emerging from the formation of the Kondo singlet.

Within the experimental uncertainty, the temperature dependencies of the XMCD intensity of peaks C and E are

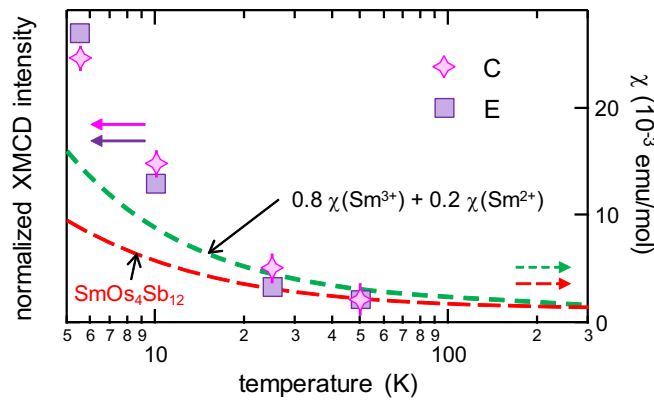


FIG. 3. Temperature dependence of the XMCD amplitude of features C and E in Fig. 1(c) (full markers, left axis) compared with the magnetic susceptibility  $\chi$  of  $\text{SmOs}_4\text{Sb}_{12}$  [18] (right axis). Also shown is a linear combination of  $\chi$  curves for  $\text{Sm}^{3+}$  and  $\text{Sm}^{2+}$  free ions in Fig. 1(g) with weights of 0.8 and 0.2, respectively.

equivalent as shown in Fig. 3. Additionally, we incorporate the combination of  $\chi$  with a  $\text{Sm}^{3+}/\text{Sm}^{2+}$  free-ion ratio of 0.8/0.2 in Fig. 3. This ratio is adopted from a previous theoretical study [35] as described below. The deviation between the two  $\chi$  curves at low temperatures is only partially accounted for by a cubic CEF splitting of 19 K deduced from isothermal magnetization measurements [41]. This strongly suggests the importance of the hybridization (or off-diagonal matrix element) effect between the  $\text{Sm}^{3+}$  and  $\text{Sm}^{2+}$  configurations, consistent with the XMCD observations.

### B. Comparison between experimental and theoretical XMCD spectra

Now we compare the experimental XMCD spectra in Fig. 4(a) [replotted from Fig. 1(c)] with theoretical calculations reported by Nanba *et al.* as shown in Fig. 4(b) [35]. The theoretical spectra were calculated for a nonmagnetic singlet ( $F^6$ ) and magnetic ( $F^5$ ) IV ground states (GSs) under  $H = 10$  T at  $T = 0$  K.

The  $F^6$  ( $F^5$ ) GS is given by a quantum mechanical mixture of  $4f^6$  ( $4f^5$ ) and  $4f^5\bar{C}$  ( $4f^6\bar{L}$ ) configurations, where  $\bar{C}$  ( $\bar{L}$ ) denotes an electron (a hole) transferred into the empty conduction (filled valence) band. In these variational approaches of the AIM, the  $4f$  orbitals on a Sm ion hybridizes with other band states with the same  $f$  symmetry [13]. A  $F^6$ -type GS with  $J = 0$  [45] is considered to accurately describe local Kondo singlet states, while a  $F^5$ -type GS with  $J \neq 0$  is considered to be suitable for describing the other limit of the local-moment RKKY regime [22,46,47]. Such  $F^6$ - and  $F^5$ -like GSs are sometimes referred to as an accompany- and transfer-type valence fluctuation states, respectively [48]. The GS of the IV compound  $\text{SmB}_6$  has been proposed to be  $F^6$ -like [47,48].

The theoretical spectra in Fig. 4(b) have been derived from conventional AIM calculations including the CEF interaction for analyzing experimental results of Sm  $3d$  HAXPES, and XAS spectra at the Sm  $M_5$  and  $L_3$  edges, which consistently result in a Sm valence of 2.8 at low temperature. Nanba *et al.* concluded in favor of the  $F^6$  GS for the description of the

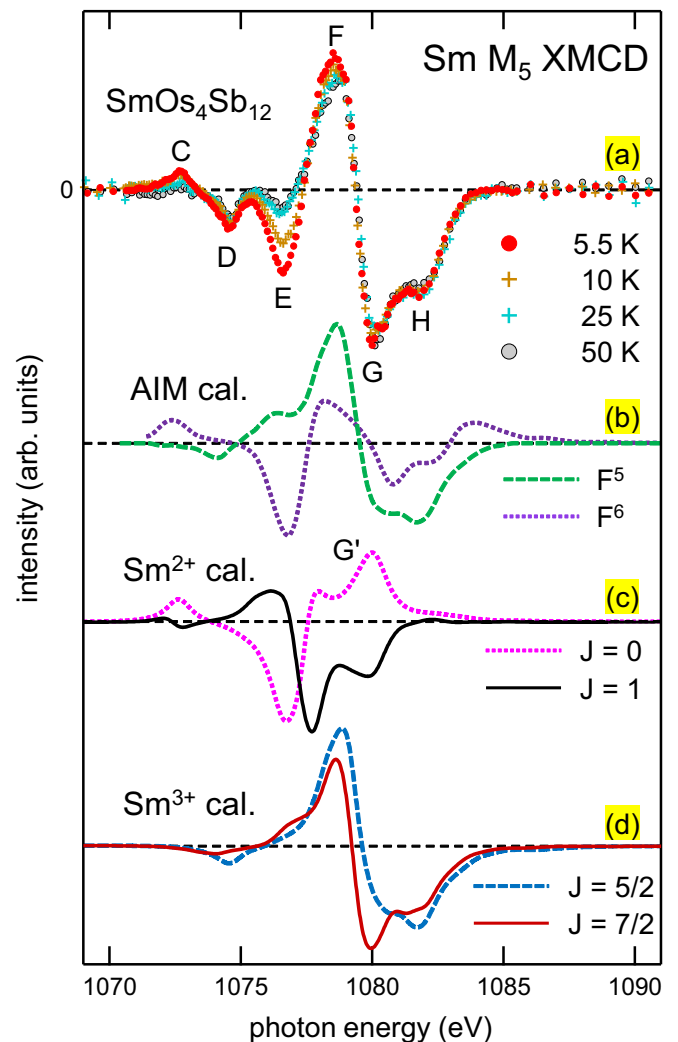


FIG. 4. Comparison of (a) the experimental Sm  $M_5$  XMCD spectra replotted from Fig. 1(c) with (d) the theoretical XMCD spectra for a magnetic ( $F^5$ ) and nonmagnetic ( $F^6$ ) ground states predicted for  $\text{SmOs}_4\text{Sb}_{12}$  [35]. Also shown are atomic multiplet calculations for (c) the  $J = 0$  and 1 states of  $\text{Sm}^{2+}$ , and (d) the  $J = 5/2$  and  $7/2$  states of  $\text{Sm}^{3+}$ .

field-insensitive HF state in  $\text{SmOs}_4\text{Sb}_{12}$  [35]. The calculated XMCD curves result from practically identical XAS spectra (not shown), both of which are in good agreement with our XAS data. The difference in XMCD line shape between the  $F^6$  and  $F^5$  curves implies that XMCD is a sensitive probe of the magnetic character of the IV state in  $\text{SmOs}_4\text{Sb}_{12}$ .

Comparison of Fig. 1(e) with Fig. 4(b) shows that the XMCD curves for the  $F^5$  and  $F^6$  GSs resemble those for the  $\text{Sm}^{3+}$  and  $\text{Sm}^{2+}$  reference spectra, respectively, with an important difference between the  $F^6$  and  $\text{Sm}^{2+}$  curves above 1080 eV. Although the origin of the difference is not included in Ref. [35], it can be understood in analogy to the case of IV Ce compounds using atomic spectral calculations as described below.

The Kondo temperature of  $\text{SmOs}_4\text{Sb}_{12}$  estimated from the Sm valence [Fig. 1(f)] is  $T_K \sim 55$  K [20], which is considered to mark the gradual crossover between the Sm  $4f$  electrons



in a magnetic state of the  $F^5$  type at high temperatures and a nonmagnetic Kondo singlet state of the  $F^6$  type at low temperatures within the conventional Kondo picture. In this picture, the Kondo singlet is almost fully formed at  $T_0$ , below which the Sm valence remains essentially unchanged (see Figs. 13 and 20 in Ref. [26]). Therefore, the XMCD shape of  $\text{SmOs}_4\text{Sb}_{12}$  is expected to be largely dominated by the  $F^6$  shape below  $T_0$ , and a gradual transformation from the  $F^6$  to  $F^5$  shapes with increasing temperature above  $T_0$ . Note that Fig. 4(b) implies that a Sm valence shift toward  $\text{Sm}^{3+}$  hardly affects the  $\text{Sm}^{3+}$ -like XMCD shape for the  $F^5$ -type state. Obviously the conventional Kondo picture in combination with the XMCD calculations is inconsistent with our data. We can, however, alternatively consider the HF (local-moment) component in the two-fluid model to be the  $F^6$  ( $F^5$ ) type GS in the AIM (see the Appendix).

It is clear from the comparison of Figs. 4(a) and 4(b) that the experimental XMCD data are adequately described by neither of the AIM calculations, but appear to be intermediate between the  $F^5$  and  $F^6$  curves. The XMCD data above  $T_0$  fall close to the  $F^5$  curve, and an admixture of the  $F^6$  contribution into the  $F^5$  curve appears appropriate for describing them in terms of the negative signal of feature E and the G/H intensity ratio of larger than 1. In addition, the gradual spectral weight transfer into the C, E, and F features observed below  $T_0$  is approximately accounted for by a gradual increase of the  $F^6$  amplitude, which strongly suggests the formation of the Kondo singlet.

We should note here that the two XMCD spectra in Fig. 4(b) are arbitrarily scaled for comparison in shape (see Fig. 6 in Ref. [35]), since these calculations employing the large-degeneracy expansion method are valid for  $T = 0$  K [49]. The  $F^5$  XMCD originates from an atomlike  $J \neq 0$  local moment that is fully magnetized in the weak-field limit at  $T = 0$  K due to the Zeeman effect, as typically described using the Brillouin function for the magnetic response [37]. Then, the paramagnetic susceptibility  $\chi(T)$  from the  $F^5$  GS is considered to show basically Curie-Weiss ( $1/T$ ) behavior with a possible modification caused by the CEF [50]. This is a strongly decreasing function of temperature analogous to that for  $\text{Sm}^{3+}$  [Fig. 1(g)]. This temperature dependence is generally consistent with the peak G behavior in Fig. 1(g).

On the other hand, the  $F^6$  GS yields only a small amount of XMCD originating from a Van Vleck type paramagnetism [49]. This magnetic moment induced by the applied field is inversely proportional to the energy separation between the singlet GS and the magnetic excited states similar to the  $\text{Sm}^{2+}$  or  $\text{Eu}^{3+}$  cases [38,51]. The  $F^6$  GS has low-lying magnetic excited states of the  $J = 1$  and  $5/2$  levels for  $\text{Sm}^{2+}$  and  $\text{Sm}^{3+}$ , respectively, and the lowest excitation is on the order of  $k_B T_K$ , where  $k_B$  is the Boltzmann constant, as determined by the details of the hybridization effect in the presence of the finite intra-atomic  $ff$  Coulomb repulsion [13,49,50]. The  $F^6$  GS is also analogous to the case of the nonmagnetic singlet GS of Ce given by a quantum mechanical mixture of  $4f^0$  and  $4f^1\bar{L}$  configurations [11,49,52,53]. Previous studies for Ce compounds suggest that  $\chi(T)$  for the  $F^6$ -type GS increases quadratically with temperature [50,54–56]. This is clearly inconsistent with the peak E behavior in Fig. 1(g), indicating that the conventional Kondo picture as well as the simple IV picture fails to describe our experimental findings.

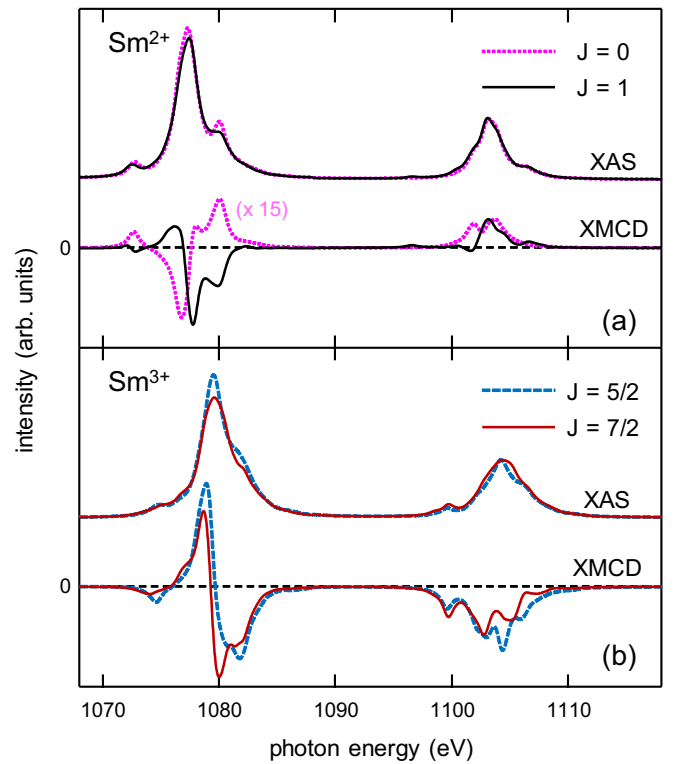


FIG. 5. Polarization averaged isotropic XAS and XMCD spectra calculated for the Sm  $M_{4,5}$  edges of (a) the  $J = 0$  and 1 states of  $\text{Sm}^{2+}$ , and (b) the  $J = 5/2$  and  $7/2$  states of  $\text{Sm}^{3+}$ .

It is important to recall that the observed two-constituent XMCD behavior below  $T_0$  in  $\text{SmOs}_4\text{Sb}_{12}$  is characterized by a progressive weight transfer from the  $F^5$ -like signal to the additional  $F^6$ -like signal [Figs. 4(a) and 4(b)]. Also, the XMCD intensity of feature G (E) representative of the  $F^5$  ( $F^6$ )-like signal shows a temperature dependence with a negative (positive) deviation from  $\chi(T)$  of the bulk below  $T_0$  [Fig. 1(g)]. Hence, our XMCD findings are approvingly accommodated by Eqs. (A.1) and (A.2) in the existing two-fluid model with a hybridization effectiveness of  $f_0 < 1$  for a temperature scale of  $T^* \approx T_0 \neq T_K$ , since the  $F^5$  ( $F^6$ )-like signal is closely connected to  $\chi_{LM}$  ( $\chi_{HF}$ ). This is consistent with a previous study of the NQR rate  $1/T_1$  of  $^{123}\text{Sb}$  on  $\text{SmOs}_4\text{Sb}_{12}$  that suggests

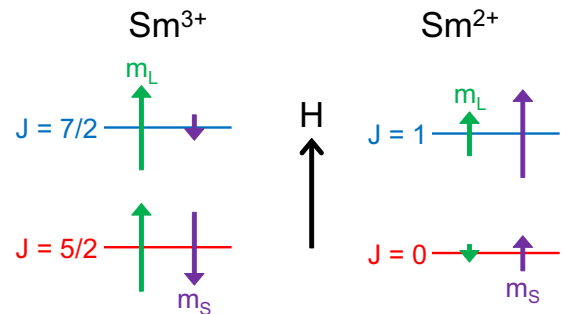


FIG. 6. Schematic illustration of the directions of the orbital ( $m_L$ ) and spin ( $m_S$ ) magnetic moments for the  $J = 5/2$  and  $7/2$  states of  $\text{Sm}^{3+}$ , and the  $J = 0$  and 1 states of  $\text{Sm}^{2+}$  aligned by the external magnetic field  $H$ .

local-moment behavior from  $\sim 50$  K down to  $T_0$ , followed by a progressive Kondo singlet formation below  $T_0$  down to  $T_C \approx 2.6$  K [24]. In other words, our findings reveal a realization of a microscopic coexistence of the dichotomic two constituents in  $\text{SmOs}_4\text{Sb}_{12}$ , both of which are capable of being approximately derived as the variational  $F^5$ - and  $F^6$ -GS wave functions for the AIM. Besides, similar XMCD investigations on IV Sm compounds with  $f_0 > 1$ , or without magnetic order, allow pure  $F^6$ -type singlet GSs to be revealed, which would be very useful for theoretical spectroscopic models.

For a better understanding of the measured XMCD spectra, we performed atomic multiplet calculations [32,42] on  $\text{Sm}^{2+}$  ( $\text{Sm}^{3+}$ ) for the  $J = 0$  and 1 ( $J = 5/2$  and  $7/2$ ) states under  $H = 10$  T, similarly to the case of  $\text{Ce}^{3+}$  [53], as shown in Fig. 5. The atomic multiplet calculations were obtained using the XTLS 9.0 program [57] for the  $3d \rightarrow 4f$  electric-dipole allowed transitions with the intra-atomic parameters given in Ref. [42], and a Lorentzian broadening of  $2\Gamma = 1$  eV. The spectra for  $J = 0$  and  $5/2$  (Hund's rules GSs) are consistent with previous calculations [40,43], and also with the experimental  $\text{Sm}^{2+}$  and  $\text{Sm}^{3+}$  references in Figs. 1(d) and 1(e).

In Figs. 4(c) and 4(d) we show the Sm  $M_5$  XMCD calculations scaled arbitrarily for visual convenience. Figure 4(c) suggests that the  $F^6$  spectral shape in Fig. 4(b) is modified from the  $J = 0$  shape by the contribution from either the  $J = 1$  level of  $\text{Sm}^{2+}$  or the  $J = 5/2$  level of  $\text{Sm}^{3+}$ , or both, by considering quantum-mechanical interference effects of configuration mixing in the initial and final states in the XA process [52,53]. This is qualitatively consistent with the absence of the G' feature [Fig. 1(e)] below  $T_0$  observed in Fig. 4(a). Also, the  $J = 7/2$  XMCD in Fig. 4(d) can account for the observed G/H intensity ratio. Besides, the  $J = 7/2$  contribution shown in Fig. 5(b) is useful in understanding the Sm  $M_4$  edge XMCD shape of  $\text{SmOs}_4\text{Sb}_{12}$  in Fig. 2. As mentioned above, these hybridization effects are analogs to the case of IV Ce materials, in which the XMCD shape derived from the  $J = 5/2$  GS of  $\text{Ce}^{3+}$  is modified by the contributions to the singlet GS from higher lying  $J = 7/2$  states of  $\text{Ce}^{3+}$ . Such mixing is possible for the case in which the hybridization strength  $V$  is comparable to or larger than the energy separation between the  $J = 5/2$  and  $7/2$  levels determined by the  $4f$  spin-orbit interaction (see Fig. 1 in Ref. [52], and Figs. 2 and 3 in Ref. [53]). Our multiplet calculation yields an energy separation of 41 (141) meV between the  $J = 0$  ( $5/2$ ) and 1 ( $7/2$ ) levels for  $\text{Sm}^{2+}$  ( $\text{Sm}^{3+}$ ). The apparent negative XMCD peaks above 1080 eV in the  $F^6$  curve and the G/H ratio in the  $F^5$  curve in Fig. 4(b), both of which contrast with our XMCD findings, highly suggest that a  $V$  value of 40 (60) meV used in the  $F^6$  ( $F^5$ ) calculation [35] is overestimated (underestimated). More importantly, our experimental results provide detailed insights into the temperature-dependent hybridization effect in  $\text{SmOs}_4\text{Sb}_{12}$  through the visualization of the final-state multiplets in the XMCD spectra.

### C. Sum-rule analysis

Our atomic multiplet calculations in Fig. 5 further provide important information on the quantities in the XMCD sum

TABLE I. Valence and  $J$  dependent values of  $m_S$ ,  $m_L$ ,  $m_S/m_L$ ,  $m_{\text{total}}$ ,  $\langle T_z \rangle / \langle S_z \rangle$ , and  $C$  obtained from our atomic multiplet calculations for  $H = 10$  T.  $m_S$ ,  $m_L$ , and  $m_{\text{total}}$  are given in units of  $\mu_B/\text{Sm}$ .

	$J$	$m_S$	$m_L$	$m_S/m_L$	$m_{\text{total}}$	$\langle T_z \rangle / \langle S_z \rangle$	$C$
$\text{Sm}^{2+}$	0	0.212	-0.106	-2	0.106	-0.237	1.50
$\text{Sm}^{2+}$	1	1.07	0.467	2.28	1.53	0.464	0.957
$\text{Sm}^{3+}$	5/2	-3.48	4.24	-0.821	0.760	-0.221	3.37
$\text{Sm}^{3+}$	7/2	-1.17	4.09	-0.287	2.91	-0.552	-2.89

rules [58–60] given by

$$\langle L_z \rangle = \frac{q(14 - n_f)}{r}, \quad (1)$$

$$\frac{\langle S_z \rangle}{\langle L_z \rangle} = \frac{5p/q - 3}{4C} \left( 1 + 3 \frac{\langle T_z \rangle}{\langle S_z \rangle} \right)^{-1}, \quad (2)$$

where  $p$  ( $q$ ) is the integral of the XMCD signal over the  $M_5$  edge ( $M_{4,5}$  edges),  $r$  is the integral of the polarization-averaged XAS intensity over the  $M_{4,5}$  edges, and  $n_f$  is the Sm  $4f$  occupation number.  $C$  is the correction factor due to the large  $jj$  mixing between  $3d_{5/2}$  and  $3d_{3/2}$  core levels [60], and  $\langle T_z \rangle$  is the magnetic dipole term. Here we use the conventional description of the orbital ( $m_L = -\langle L_z \rangle$ ) and spin ( $m_S = -2\langle S_z \rangle$ ) moments.

Table I summaries the calculated values for  $m_S$ ,  $m_L$ ,  $m_S/m_L$ , the total atomic moment ( $m_{\text{total}} = m_L + m_S$ ),  $\langle T_z \rangle / \langle S_z \rangle$ , and  $C$  for the  $J = 0$  and 1 states of  $\text{Sm}^{2+}$ , and the  $J = 5/2$  and  $7/2$  states of  $\text{Sm}^{3+}$ . The results for the  $J = 5/2$  state in  $\text{Sm}^{3+}$  agree well with a previous study [60]. This table indicates that the application of the second sum rule for IV Sm systems is typically complicated by the valence and  $J$ -term dependencies in  $\langle T_z \rangle / \langle S_z \rangle$  and  $C$ .

The experimental spectra at 5.5 K (Fig. 2) provide  $q/r = -0.010$  and  $p/q = 0.59$  with an expected systematic error of approximately  $\pm 10\%$ . Then the sum rule analysis with  $n_f = 5.2$  yields  $m_L = 0.092 \mu_B/\text{Sm}$ , and  $m_S/m_L \approx 0$  since the term  $5p/q - 3$  is close to zero. This, in turn, results in  $m_{\text{total}} \approx m_L$ , which is close to a magnetic moment of  $0.102 \mu_B/\text{Sm}$  determined from bulk magnetometry under the same conditions [41]. Such an unusually small  $m_S/m_L$  ratio in the strongly hybridized Sm  $4f$  state can be accounted for by the configuration dependent magnetic alignments given in Table I, and shown schematically in Fig. 6. It should be noted here that the Van Vleck paramagnetism of the  $\text{Sm}^{2+}$   $J = 0$  GS is characterized by  $m_{\text{total}} = m_S/2 = -m_L$  [61]. Since the direction of  $m_{\text{total}}$  is aligned parallel to the field  $H$ , the  $m_S$  moments of  $\text{Sm}^{2+}$  and  $\text{Sm}^{3+}$  point in opposite directions. This is likely to cause  $m_S/m_L$  to approach zero. Figure 6 provides a basis for the hybridization effect on the magnetic properties of IV Sm compounds. Further XMCD studies at low temperatures and theoretical investigations prove to be insightful for clarifying the origin of the field-insensitive ferromagnetic HF state in  $\text{SmOs}_4\text{Sb}_{12}$ .

### IV. CONCLUSION

To conclude, motivated by the theoretical predictions by Namba *et al.*, we have used an element- and orbital-specific probe of XMCD at the Sm  $M_5$  absorption edge on  $\text{SmOs}_4\text{Sb}_{12}$ ,

and successfully observed a distinct temperature evolution of the Kondo effect on the  $4f$  moments across  $T_0 \approx 20$  K. This is consistent with reported NQR measurements, although it does not conform to the conventional Kondo picture. The Sm  $4f$  states in this material go beyond a simple incoherent IV picture for even above  $T_0$ . The XMCD component emerging additionally below  $T_0$  under a constant IV Sm valence has its origin in the Kondo singlet with a magnetic state largely dominated by the  $\text{Sm}^{2+}$  character, while the local-moment component with a constant XMCD shape observed over the measured range below 50 K comes from an IV Sm state with a magnetic moment analogous to that of  $\text{Sm}^{3+}$ . A combination of reported XMCD predictions and the two-fluid model is found to be useful in describing our results. This work demonstrates the applicability of the XMCD in the soft x-ray region, and reveals microscopic details of complicated configuration-mixing effects in  $\text{SmOs}_4\text{Sb}_{12}$  and the two-fluid phenomenology. Our observations provide an important benchmark for future studies that lead to elucidate the complication of KL materials.

#### ACKNOWLEDGMENTS

The authors thank K. Nagai, S. Fujioka, Y. Aoyama, S. Hamamoto, Y. Kanai-Nakata, D. Iwasaki, Y. Higashino, and Y. Takeda for XMCD experiments. We also thank N. Sasabe for valuable discussions. Y.S. thanks A. Kimura for providing the XAS and XMCD data of  $(\text{Sm,Gd})\text{Al}_2$ . The XMCD measurements were performed under the approval of BL23SU at SPring-8 (Proposal No. 2016A3832). This work was financially supported by Grant-in-Aid for Scientific Research on Innovative Areas (Grants No. JP20102003 and No. JP16H01074), Grant-in-Aid for Young Scientists (Grant No. JP23740240), and Grant-in-Aid for Scientific Research (Grants No. JP16H04014 and No. JP18K03512) from the Ministry of Education, Culture, Sports, Science and Technology, Japan.

#### APPENDIX: PHENOMENOLOGICAL TWO-FLUID MODEL

The phenomenological two-fluid model [15] postulates that a HF fluid originating from the formation of the Kondo singlet emerges, and coexists with partially screened local moments below a temperature  $T^*$  with fractions of  $1 - f(T)$

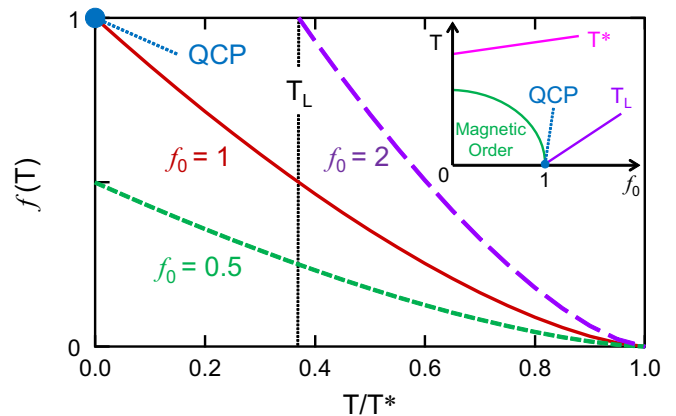


FIG. 7. Heavy fermion fraction  $f(T)$  as a function of temperature for different values of  $f_0$ . Inset: Schematic  $f_0$ - $T$  phase diagram in the two-fluid model [15].

and  $f(T)$ , respectively. The magnetic susceptibility is then given by

$$\chi(T) = [1 - f(T)]\chi_{\text{LM}} + f(T)\chi_{\text{HF}}, \quad (\text{A1})$$

where  $\chi_{\text{LM}}$  and  $\chi_{\text{HF}}$  are the local-moment and HF components, respectively. We regard  $[1 - f(T)]\chi_{\text{LM}}$  and  $f(T)\chi_{\text{HF}}$  as being proportional to the paramagnetic XMCD amplitude of the  $F^5$  and  $F^6$  states, respectively.  $T^*$  is considered to be determined not by the Kondo interaction, but by the RKKY interaction. It has been found in the paramagnetic phase of a broad range of KLs that  $f(T)$  for  $T < T^*$  is given empirically by

$$f(T) = f_0(1 - T/T^*)^{3/2}, \quad (\text{A2})$$

where the coefficient  $f_0$  is the material-dependent positive parameter called the hybridization effectiveness. Figure 7 shows  $f(T)$  curves for different values of  $f_0$ . For  $f_0 < 1$ , the local-moment fraction persists down to 0 K, leading to stabilize magnetic order at low temperatures in the presence of the RKKY interaction as shown the inset of Fig. 7. For  $f_0 > 1$ , the local moments entirely transform into the HF fluid below  $T_L$  referred to as the delocalization temperature. The crossover at  $T = 0$  K for  $f_0 = 1$  corresponds to the quantum critical point (QCP).

[1] S. Wirth and F. Steglich, *Nat. Rev. Mater.* **1**, 16051 (2016).  
 [2] P. Gegenwart, Q. Si, and F. Steglich, *Nat. Phys.* **4**, 186 (2008).  
 [3] E. Dagotto, *Science* **309**, 257 (2005).  
 [4] S. Doniach, *Physica B+C (Amsterdam)* **91**, 231 (1977); *Valence Instabilities and Related Narrow Band Phenomena*, edited by R. D. Parks (Plenum, New York, 1977), p. 1669.  
 [5] Y.-F. Yang, Z. Fisk, H.-O. Lee, J. D. Thompson, and D. Pines, *Nature (London)* **454**, 611 (2008).  
 [6] S. Ernst, S. Kirchner, C. Krellner, C. Geibel, G. Zwirgagl, F. Steglich, and S. Wirth, *Nature (London)* **474**, 362 (2011).  
 [7] S.-K. Mo, W. S. Lee, F. Schmitt, Y. L. Chen, D. H. Lu, C. Capan, D. J. Kim, Z. Fisk, C.-Q. Zhang, Z. Hussain, and Z.-X. Shen, *Phys. Rev. B* **85**, 241103(R) (2012).

[8] P. Aynajian, E. H. da Silva Neto, A. Gyenis, R. E. Baumbach, J. D. Thompson, Z. Fisk, E. D. Bauer, and A. Yazdani, *Nature (London)* **486**, 201 (2012).  
 [9] Q. Y. Chen, D. F. Xu, X. H. Niu, J. Jiang, R. Peng, H. C. Xu, C. H. P. Wen, Z. F. Ding, K. Huang, L. Shu, Y. J. Zhang, H. Lee, V. N. Strocov, M. Shi, F. Bisti, T. Schmitt, Y. B. Huang, P. Dudin, X. C. Lai, S. Kirchner, H. Q. Yuan, and D. L. Feng, *Phys. Rev. B* **96**, 045107 (2017).  
 [10] E. A. Goremychkin, H. Park, R. Osborn, S. Rosenkranz, J.-P. Castellán, V. R. Fanelli, A. D. Christianson, M. B. Stone, E. D. Bauer, K. J. McClellan, D. D. Byler, and J. M. Lawrence, *Science* **359**, 186 (2018).

- [11] A. Kotani and H. Ogasawara, *J. Electron Spectrosc. Relat. Phenom.* **60**, 257 (1992).
- [12] D. Malterre, M. Grioni, and Y. Baer, *Adv. Phys.* **45**, 299 (1996).
- [13] P. S. Riseborough and J. M. Lawrence, *Rep. Prog. Phys.* **79**, 084501 (2016).
- [14] N. J. Curro, *Rep. Prog. Phys.* **79**, 064501 (2016).
- [15] Y.-F. Yang, *Rep. Prog. Phys.* **79**, 074501 (2016).
- [16] G. Lonzarich, D. Pines, and Y. F. Yang, *Rep. Prog. Phys.* **80**, 024501 (2017).
- [17] S. Sanada, Y. Aoki, H. Aoki, A. Tsuchiya, D. Kikuchi, H. Sugawara, and H. Sato, *J. Phys. Soc. Jpn.* **74**, 246 (2005).
- [18] W. M. Yuhasz, N. A. Frederick, P. C. Ho, N. P. Butch, B. J. Taylor, T. A. Sayles, M. B. Maple, J. B. Betts, A. H. Lacerda, P. Rogl, and G. Giester, *Phys. Rev. B* **71**, 104402 (2005).
- [19] H. Sato, H. Sugawara, Y. Aoki, and H. Harima, in *Handbook of Magnetic Materials*, edited by K. H. J. Buschow (North-Holland, Amsterdam, 2009), Vol. 18, p. 1.
- [20] K. Fushiya, R. Miyazaki, R. Higashinaka, A. Yamada, M. Mizumaki, S. Tsutsui, K. Nitta, T. Uruga, B. Suemitsu, H. Sato, and Y. Aoki, *Phys. Rev. B* **92**, 075118 (2015).
- [21] R. Higashinaka, A. Yamada, T. D. Matsuda, and Y. Aoki, *AIP Adv.* **8**, 125017 (2018).
- [22] A. Yamasaki, S. Imada, H. Higashimichi, H. Fujiwara, T. Saita, T. Miyamachi, A. Sekiyama, H. Sugawara, D. Kikuchi, H. Sato, A. Higashiya, M. Yabashi, K. Tamasaku, D. Miwa, T. Ishikawa, and S. Suga, *Phys. Rev. Lett.* **98**, 156402 (2007).
- [23] S. Tsutsui, J. Nakamura, Y. Kobayashi, Y. Yoda, M. Mizumaki, A. Yamada, R. Higashinaka, T. D. Matsuda, and Y. Aoki, *J. Phys. Soc. Jpn.* **88**, 023701 (2019).
- [24] H. Kotegawa, H. Hidaka, T. C. Kobayashi, D. Kikuchi, H. Sugawara, and H. Sato, *Phys. Rev. Lett.* **99**, 156408 (2007).
- [25] Y. Aoki, S. Sanada, D. Kikuchi, H. Sugawara, and H. Sato, *J. Phys. Soc. Jpn.* **80**, SA013 (2011).
- [26] N. E. Bickers, D. L. Cox, and J. W. Wilkins, *Phys. Rev. B* **36**, 2036 (1987).
- [27] Y. Matsumoto, S. Nakatsuji, K. Kuga, Y. Karaki, N. Horie, Y. Shimura, T. Sakakibara, A. H. Nevidomskyy, and P. Coleman, *Science* **331**, 316 (2011).
- [28] K. Kummer, C. Geibel, C. Krellner, G. Zwirgagl, C. Laubschat, N. B. Brookes, and D. V. Vyalikh, *Nat. Commun.* **9**, 2011 (2018).
- [29] S. Mombetsu, T. Murazumi, H. Hidaka, T. Yanagisawa, H. Amitsuka, P.-C. Ho, and M. B. Maple, *Phys. Rev. B* **94**, 085142 (2016).
- [30] T. Funk, A. Deb, S. J. George, H. Wang, and S. P. Cramer, *Coord. Chem. Rev.* **249**, 3 (2005).
- [31] G. van der Laan and A. I. Figueroa, *Coord. Chem. Rev.* **277**, 95 (2014).
- [32] S. Imada and T. Jo, *J. Phys. Soc. Jpn.* **59**, 3358 (1990).
- [33] L. Joly, J.-P. Kappler, P. Ohresser, Ph. Sainctavit, Y. Henry, F. Gautier, G. Schmerber, D. J. Kim, C. Goyhenex, H. Boulou, O. Bengone, J. Kavich, P. Gambardella, and F. Scheurer, *Phys. Rev. B* **95**, 041108(R) (2017).
- [34] C. Praetorius and K. Fauth, *Phys. Rev. B* **95**, 115113 (2017).
- [35] Y. Nanba, M. Mizumaki, and K. Okada, *J. Phys. Soc. Jpn.* **82**, 104712 (2013).
- [36] Y. Saitoh, Y. Fukuda, Y. Takeda, H. Yamagami, S. Takahashi, Y. Asano, T. Hara, K. Shirasawa, M. Takeuchi, T. Tanaka, and H. Kitamura, *J. Synchrotron Radiat.* **19**, 388 (2012).
- [37] Y. Saitoh, A. Yasui, H. Fuchimoto, Y. Nakatani, H. Fujiwara, S. Imada, Y. Narumi, K. Kindo, M. Takahashi, T. Ebihara, and A. Sekiyama, *Phys. Rev. B* **96**, 035151 (2017).
- [38] M. B. Maple and D. Wohlleben, *Phys. Rev. Lett.* **27**, 511 (1971).
- [39] Y. Saitoh, T. Muro, M. Kotsugi, T. Iwasaki, A. Sekiyama, S. Imada, and S. Suga, *J. Synchrotron Radiat.* **8**, 339 (2001).
- [40] S. Qiao, A. Kimura, H. Adachi, K. Iori, K. Miyamoto, T. Xie, H. Namatame, M. Taniguchi, A. Tanaka, T. Muro, S. Imada, and S. Suga, *Phys. Rev. B* **70**, 134418 (2004).
- [41] Y. Aoki, S. Sanada, H. Aoki, D. Kikuchi, H. Sugawara, and H. Sato, *Physica B* **378-380**, 54 (2006).
- [42] B. T. Thole, G. van der Laan, J. C. Fuggle, G. A. Sawatzky, R. C. Karnatak, and J.-M. Esteve, *Phys. Rev. B* **32**, 5107 (1985).
- [43] W. T. Fuhrman, J. C. Leiner, J. W. Freeland, M. van Veenendaal, S. M. Koohpayeh, W. A. Phelan, T. M. McQueen, and C. Broholm, *Phys. Rev. B* **99**, 020401(R) (2019).
- [44] M. Sundermann, H. Yavas, K. Chen, D. J. Kim, Z. Fisk, D. Kasinathan, M. W. Haverkort, P. Thalmeier, A. Severing, and L. H. Tjeng, *Phys. Rev. Lett.* **120**, 016402 (2018).
- [45]  $J = |L - S|$  due to the spin-orbit coupling, where  $L$  and  $S$  are the total orbital and the total spin angular momentum, respectively. In the case of the  $F^6$  GS,  $J = |L| - |S| = 0$ .
- [46] N. Sasabe, H. Tonai, and T. Uozumi, *J. Phys. Soc. Jpn.* **86**, 093701 (2017).
- [47] S. Suga, K. Sakamoto, T. Okuda, K. Miyamoto, K. Kuroda, A. Sekiyama, J. Yamaguchi, H. Fujiwara, A. Irizawa, T. Ito, S. Kimura, T. Balashov, W. Wulfhekel, S. Yeo, F. Iga, and S. Imada, *J. Phys. Soc. Jpn.* **83**, 014705 (2013).
- [48] Q. Wu and L. Sun, *Rep. Prog. Phys.* **80**, 112501 (2017).
- [49] O. Gunnarsson and K. Schönhammer, *Phys. Scr.* **1987**, 273 (1987).
- [50] P. Schlottmann, *Phys. Rep.* **181**, 1 (1989).
- [51] Y. Takikawa, S. Ebisu, and S. Nagata, *J. Phys. Chem. Solids* **71**, 1592 (2010).
- [52] T. Jo and S. Imada, *J. Phys. Soc. Jpn.* **59**, 1421 (1990).
- [53] M. Finazzi, F. M. F. de Groot, A.-M. Dias, B. Kierren, F. Bertran, Ph. Sainctavit, J.-P. Kappler, O. Schulte, W. Felsch, and G. Krill, *Phys. Rev. Lett.* **75**, 4654 (1995).
- [54] C. M. Varma and Y. Yafet, *Phys. Rev. B* **13**, 2950 (1976).
- [55] T. V. Ramakrishnan and K. Sur, *Phys. Rev. B* **26**, 1798 (1982).
- [56] G. Zwirgagl, V. Zevin, and P. Fulde, *Z. Phys. B: Condens. Matter* **79**, 365 (1990).
- [57] A. Tanaka and T. Jo, *J. Phys. Soc. Jpn.* **63**, 2788 (1994).
- [58] B. T. Thole, P. Carra, F. Sette, and G. van der Laan, *Phys. Rev. Lett.* **68**, 1943 (1992).
- [59] P. Carra, B. T. Thole, M. Altarelli, and X. Wang, *Phys. Rev. Lett.* **70**, 694 (1993).
- [60] Y. Teramura, A. Tanaka, B. T. Thole, and T. Jo, *J. Phys. Soc. Jpn.* **65**, 3056 (1996).
- [61] M. Mizumaki, T. Uozumi, A. Agui, N. Kawamura, and M. Nakazawa, *Phys. Rev. B* **71**, 134416 (2005).